Journal of Chemical Health Risks

www.jchr.org

JCHR (2026) 16(2), 2917 - 2930

Electrochemical Performance of Green-Synthesized $CoNiO_2$ and $NdNiO_3$ Nanocomposites for Cyclic Voltammetry

1. Mrs. K. Punitha Valli, and 2*. Dr.C. Thillaiyadi Valliammai

Address: Research Scholar, A.V.V.M Sri Pushpam College (Autonomous)Poondi

2*. Associate professor of Chemistry
AVVM Sripushpam college (Autonomous) Poondi

KEYWORDS

Nickel oxide, Hydrothermal cyclic voltammetry.

ABSTRACT:

Using a straightforward hydrothermal synthesis technique, cobalt nickel oxide ($CoNiO_2$) and neodymium nickel oxide ($NdNiO_3$) nanocomposites were effectively created. A variety of analytical methods, such as X-ray diffraction (XRD), Fourier-transform infrared spectroscopy (FT-IR), scanning electron microscopy (SEM), X-ray photoelectron spectroscopy (XPS), and UV-visible diffuse reflectance spectroscopy (UV-DRS), were used to thoroughly examine these nanocomposites. For NiO, $CoNiO_2$, and $NdNiO_3$, the observed crystallite sizes were around 43.5 nm, 46.3 nm, and 56.2 nm, respectively. Different morphological characteristics were discovered by SEM examination; $NdNiO_3$ had a distinctive flower-like morphology, whereas $CoNiO_2$ displayed an agglomerated structure. Using the Kubelka-Munk method on UV-DRS data, the optical band gaps were determined to be 3.0 eV for $CoNiO_2$ and 2.7 eV for $NdNiO_3$. Both nanocomposites were subjected to electrochemical performance experiments; $NdNiO_3$ demonstrated better electrochemical behaviour than $CoNiO_2$.

Introduction

Because of their distinct physicochemical characteristics, structural variety, and high surface activity, transition metal oxides and their nanocomposites have garnered a lot of interest recently in the domains of energy storage, catalysis, and electronic devices. Due to their superior electrochemical, corrosion-resistant, and thermal stability, nickel-based oxides in particular, nickel oxide (NiO) have been extensively studied. However, other metal elements can greatly improve NiO's performance, resulting in the creation of doped or bimetallic nanostructures with increased surface area, redox activity, and conductivity. Because of the synergistic interaction between cobalt and nickel ions, which improves electron transport and electrochemical performance, cobalt nickel oxide ($CoNiO_2$) has become a promising material. Neodymium nickel oxide ($NdNiO_3$) and other rare-earth metal-doped nickel oxides are also attracting attention because of their distinctive electrical structure, small band gap, and potent hybridisation between Ni 3d and O 2p orbitals, all of which are advantageous for a range of electronic and catalytic applications.

Experimental

1.1. Materials

In this study the required chemicals such as Graphite powder, Sodium nitrate, Sulphuric acid, Potassium permanganate, Nickel nitrate ($Ni(NO_3)_2$), Cobalt chloride hexahydrate ($CoCl_2.6H_2O$), Neodymium nitrate hexahydrate ($Nd(NO_3)_3 \cdot 6H_2O$), Oxalic acid and Hydrogen peroxide were in the analytical grade and used as such without any further purification.

Synthesis of Nickel Oxide

A hydrothermal method was used to create nickel oxide. In order to create a homogenous solution, 2.33 g of nickel nitrate [$Ni(NO_3)_2$] and 0.16 g of oxalic acid were dissolved in 70 mL of distilled water and constantly agitated for 30 minutes at room temperature. After that, this solution was cooked for 12 hours at 120°C in a stainless-steel autoclave lined

Journal of Chemical Health Risks
www.jchr.org
JCHR (2026) 16(2), 2917 - 2930

with Teflon. To get rid of any remaining contaminants, the reaction's resultant solid was carefully washed with distilled water and ethanol. After cleaning, the product was allowed to air dry at 80°C. To get appropriate crystallization and phase formation, the dry material was next thermally treated in a muffle furnace for five hours at 400°C.

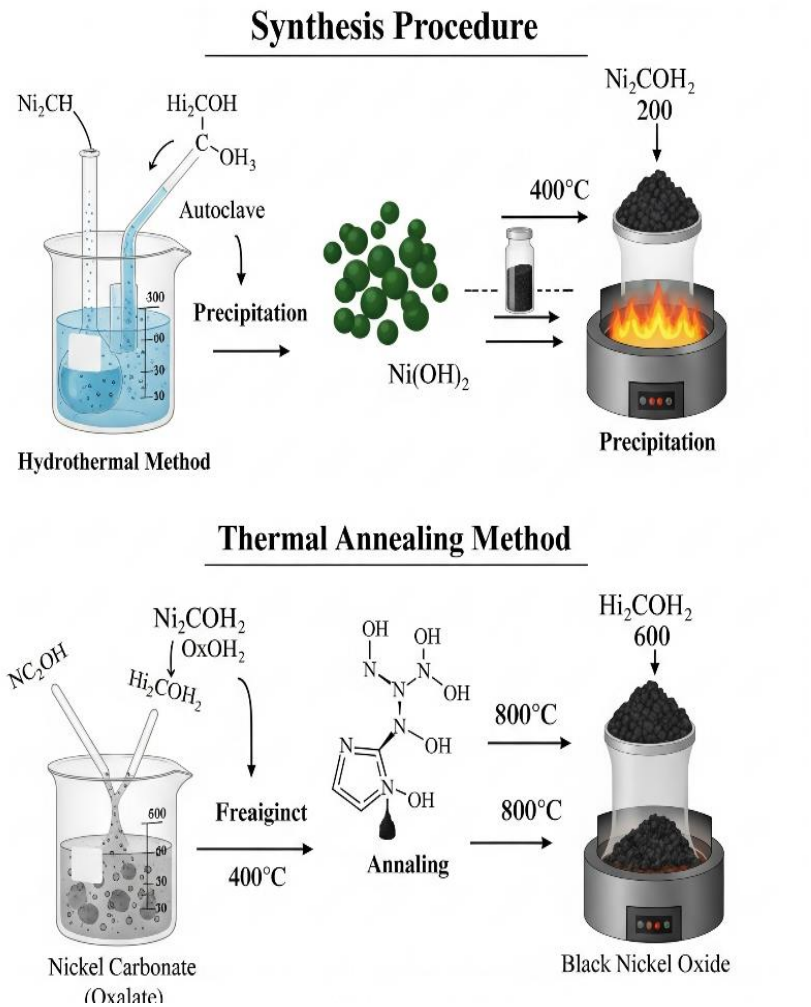

Fig. 1.2. Synthesis of Nickel Oxide

1.2. Synthesis of $CoNiO_2$ Nanocomposite

The $CoNiO_2$ nanocomposite was created by dissolving 3.46 g of nickel nitrate hexahydrate [$Ni(NO_3)_2 \cdot 6H_2O$] and 0.7 g of sodium hydroxide (NaOH) in 60 mL of distilled water while stirring constantly. 1.9 g of cobalt chloride hexahydrate [$CoCl_2 \cdot 6H_2O$] was progressively added to the solution after it had completely dissolved. To guarantee homogeneity, the mixture was agitated for half an hour at room temperature. After that, it was placed into a stainless-steel autoclave lined with Teflon and heated to 120°C for 12 hours. Following completion, unreacted ions and other contaminants were removed from the solid product by filtering and thoroughly washing it with distilled water and ethanol. To improve crystallinity, the cleaned material was calcined in a muffle furnace for five hours at 450°C after being dried at 80°C with ambient air. The cobalt nickel oxide ($CoNiO_2$) nanocomposite was the end result.

Journal of Chemical Health Risks
www.jchr.org
JCHR (2026) 16(2), 2917 - 2930

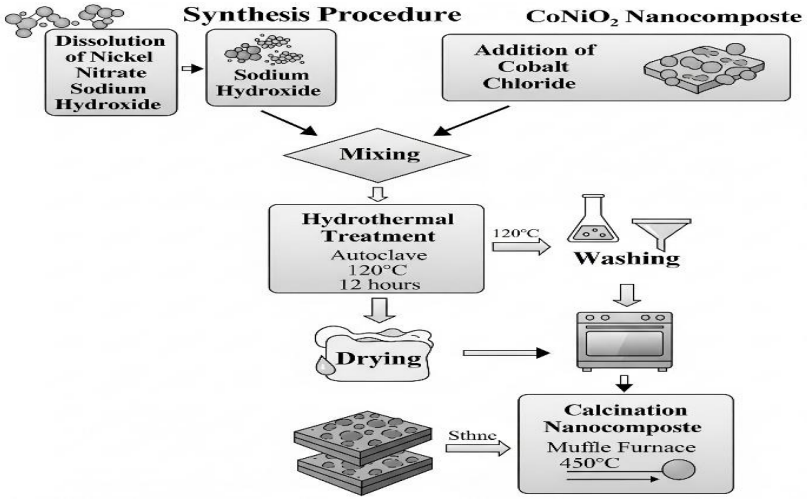

Fig. 2 Synthesis of $CoNiO_2$ Nanocomposite

1.6. Synthesis of $CoNiO_2$ and $NdNiO_3$ Nanocomposite

2.37 g of nickel nitrate hexahydrate [$Ni(NO_3)_2 \cdot 6H_2O$] and 0.3 g of sodium hydroxide (NaOH) were dissolved in 60 mL of distilled water while being continuously stirred to create the $CoNiO_2$ nanocomposite. 4.38 g of neodymium nitrate hexahydrate [$Nd(NO_3)_3 \cdot 6H_2O$] was progressively added to the solution after it had been well combined. To guarantee homogeneity, the mixture was agitated for half an hour at room temperature. After that, the resultant solution was put into an autoclave lined with Teflon and heated to 120°C for 12 hours. Following the reaction, the precipitate was collected and extensively cleaned with ethanol and distilled water to get rid of any remaining ions or byproducts. After being cleaned, the material was thermally annealed in a muffle furnace for five hours at 450°C after being dried in air at 80°C. The intended $NdNiO_3$ nanocomposite was produced by this technique.

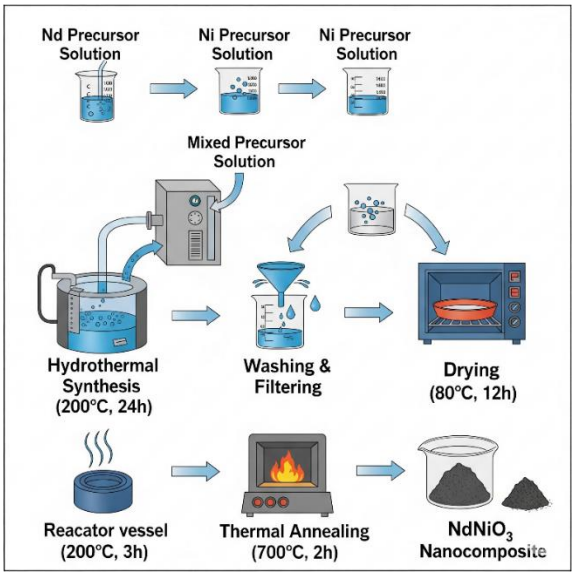

Fig. 3 Synthesis of $NdNiO_3$ nanocomposite

Journal of Chemical Health Risks
www.jchr.org
JCHR (2026) 16(2), 2917 - 2930

2. Characterization

2.1 XRD Analysis

Following heat treatment at 450°C, the synthesized samples were subjected to X-ray diffraction (XRD) examination to examine their crystalline structure. According to the standard data in JCPDS Card No. 89-7390, the diffraction peaks for NiO nanoparticles were in agreement with the (311), (222), (220), (200), (111), and (004) crystal planes. The XRD pattern for the $CoNiO_2$ composite showed clear reflections at the (004), (200), (220), (311), (400), (422), and (511) planes, which were in good agreement with JCPDS Card No. 10-0188 [14]. As per the reference pattern from JCPDS Card No. 41-0344 [15], the XRD peaks for $NdNiO_3$ were also attributed to the (002), (011), (012), (110), (103), and (511) planes. The effective creation of the $CoNiO_2$ and $NdNiO_3$ nanostructures at about 450°C is confirmed by the appearance of these distinctive peaks upon calcination. As seen in Fig. 1, the phase purity of the synthesized materials is indicated by the lack of any secondary or unknown peaks. Additionally, the Debye–Scherrer equation (Equation 1) was used to determine the average crystallite sizes of $CoNiO_2$ and $NdNiO_3$. The findings are shown in Table 1

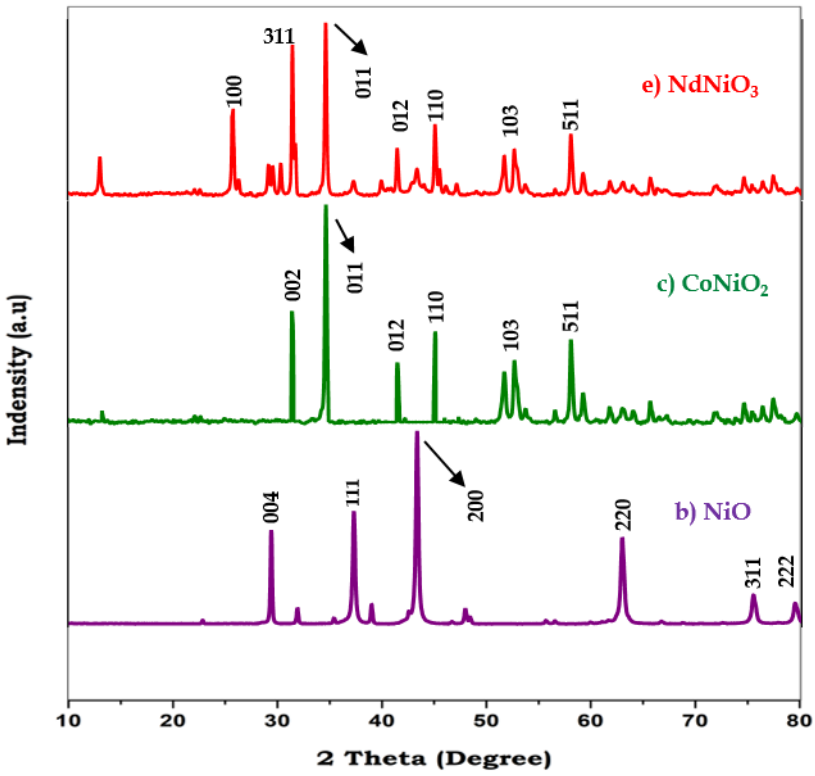

Fig.1 XRD spectra of (a)NiO (b) $CoNiO_2$ (c)$CoNiO_2$.

The crystalline size of the nanocomposites is calculated using the following Debye–Scherer's equation

$$\text{Crystalline size (D)} = \frac{0.9\lambda}{\beta \cos\theta} \quad \text{------ (1)}$$

Where λ is the wavelength (λ = 1.5406 Å (Cu Kα), β is the full width half maximum (FWHM) and θ is the diffraction angle.

Journal of Chemical Health Risks
www.jchr.org
JCHR (2026) 16(2), 2917 - 2930

Table.1. Crystalline size of (a)NiO (b)CoNiO2 (c)CoNiO2

S.No	Sample	Crystaline Size(nm)
1.	NiO	43.5
2.	$CoNiO_2$	46.3
3.	$NdNiO_3$	**64.5**

2.2 Functional group analysis

The many functional groups present in prepared materials, including those containing oxygen, may be effectively analysed using the FT-IR approach. The well oxidation of the NiO was verified by the FT-IR spectra of NiO displayed in Fig. 2a, with peaks appearing at 616 and 663 cm^{-1}. The stretching mode of the H-O-H group of NiO is responsible for the vibration band seen at 3438 cm^{-1}, as seen in Fig. 2a. The stretching mode of the Ni-O bond in the CoNiO material is responsible for the stretching vibrations' peaks at 589 and 645 cm^{-1} (Fig. 2b). The $NdNiO_3$ composite exhibits a synergistic impact to increase the catalytic activity of the nanocomposite. The Ni-O band occurred at 605 and 638 cm^{-1}, while the H-O-H stretching vibrations peak appeared at 3512 cm^{-1}, respectively (Fig. 2c).

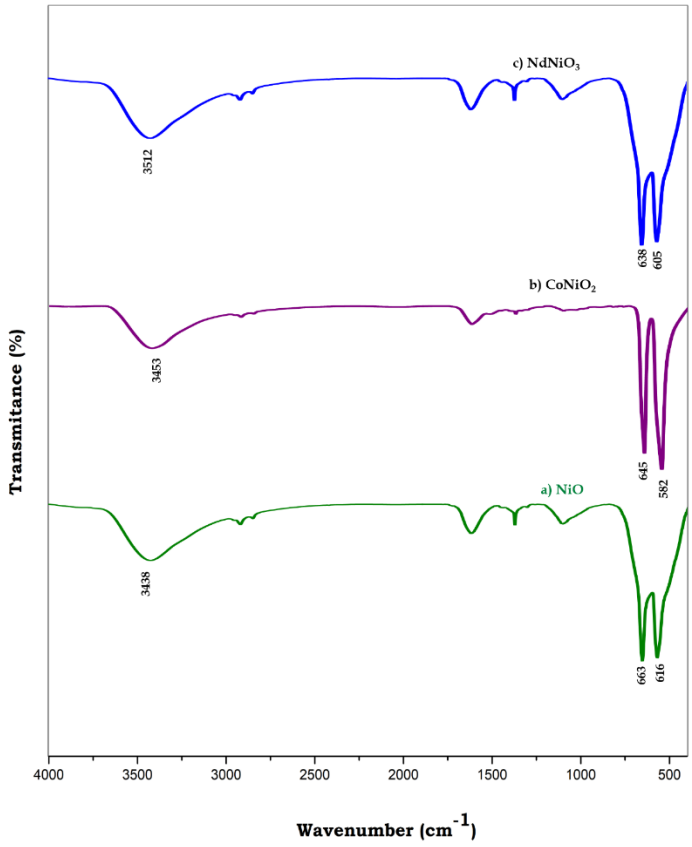

Fig. 2 FT-IR Spectra of (a)NiO (b)$CoNiO_2$ (c)$NdNiO_3$

Journal of Chemical Health Risks
www.jchr.org
JCHR (2026) 16(2), 2917 - 2930

2.3 Morphology Analysis

Using scanning electron microscopy (SEM), the surface properties of the synthesised NiO, $CoNiO_2$, and $NdNiO_3$ nanoparticles were investigated, as shown in Fig. 3a–f. According to the SEM pictures, there is a significant degree of agglomeration because NiO particles have a tendency to group together. Similarly, as seen in Fig. 3c, the $CoNiO_2$ sample likewise displayed a noticeably agglomerated appearance. On the other hand, a clear flower-like nanostructure was seen in the SEM picture of $NdNiO_3$ (Fig. 3d), indicating a more sophisticated and ordered surface architecture.

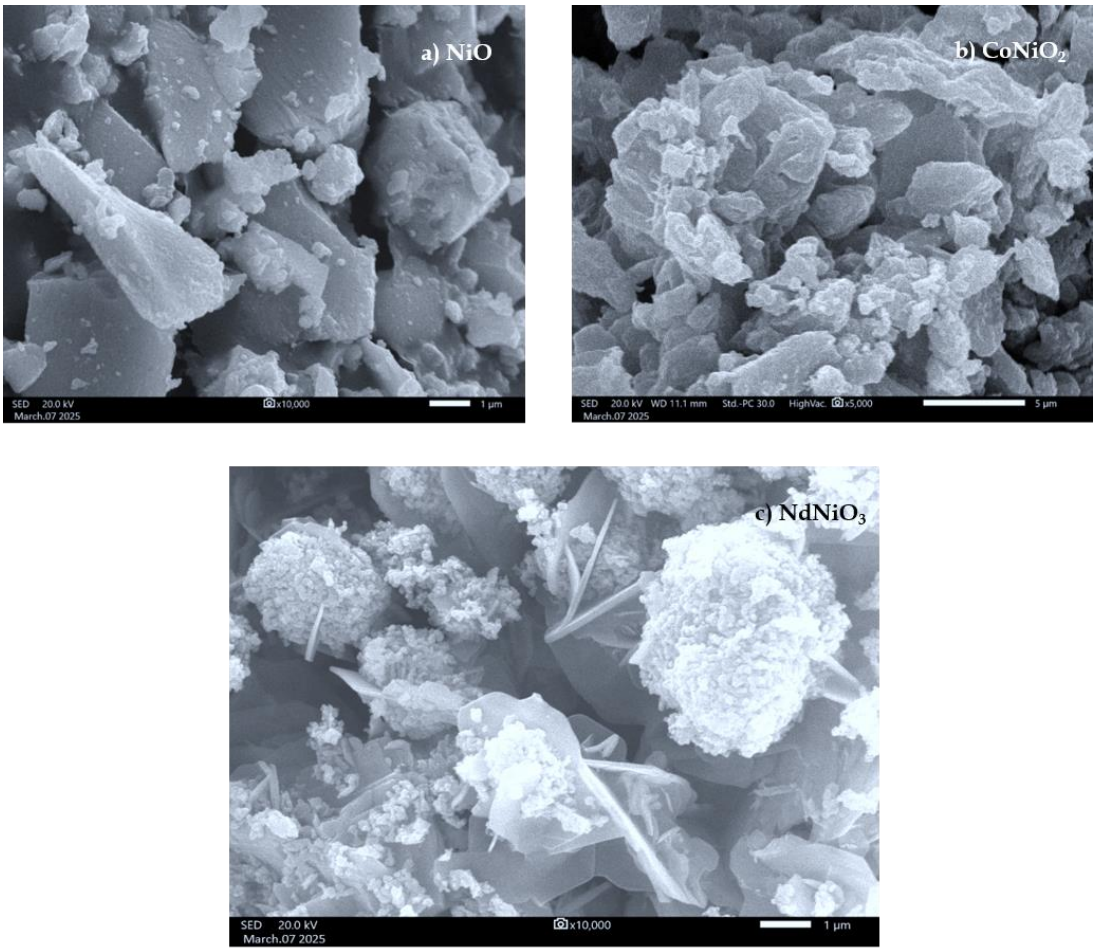

Fig.3 SEM analysis (a)NiO (b)$CoNiO_2$ (c)$NdNiO_3$ Nanomaterials

2.4 UV - DRS Analysis

UV–visible diffuse reflectance spectroscopy (UV-DRS) was used to investigate the optical characteristics of $CoNiO_2$ and $NdNiO_3$ nanocomposites, as shown in Fig. 4. Both materials demonstrated effective light absorption in the visible to near-infrared spectrum, with significant absorption margins around 800 nm. The absorption edges for these nanocomposites were moved towards longer wavelengths compared to other samples, indicating changes in their electronic structures. Changes in the materials' band structure are reflected in the movements in the absorption edge.

Journal of Chemical Health Risks
www.jchr.org
JCHR (2026) 16(2), 2917 - 2930

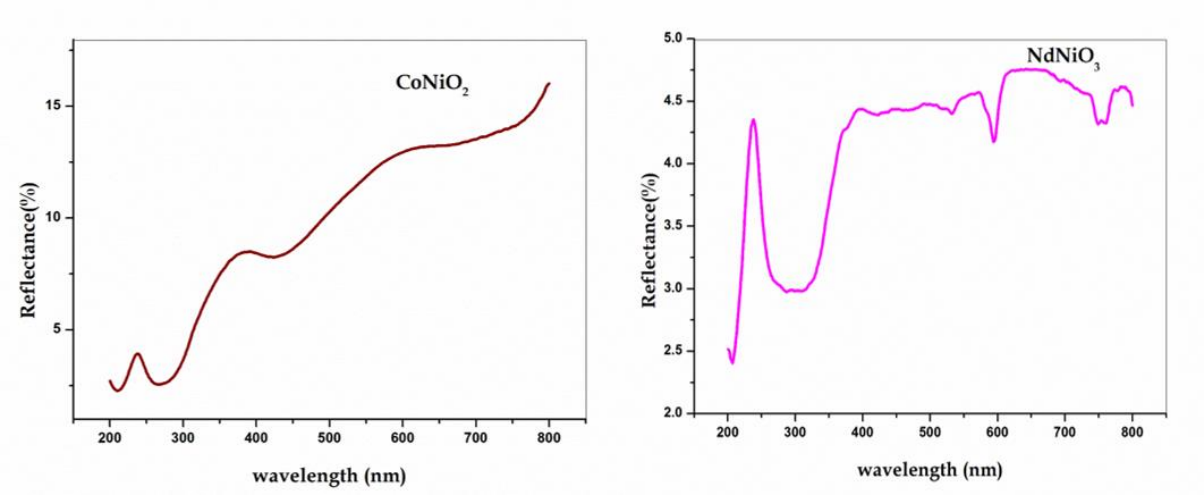

Fig.4 UV-DRS spectrum of (a) $CoNiO_2$ and (b) $NdNiO_3$

Equation (2) was used to apply the Kubelka–Munk function in order to further analyse the optical band gap

$$A(h\nu - Eg)^n \quad (2) = \alpha h\nu$$

In this case, n is dependent on the kind of electronic transition, α is the absorption coefficient, hν is the photon energy, and Eg is the band gap energy. The linear part of the graphs was extrapolated to the energy axis to produce the band gap values, as shown in Fig. 5. For $CoNiO_2$ and $NdNiO_3$, the determined band gap energies were 3.0 eV and 2.7 eV, respectively. Oxygen vacancies, which bring impurity states close to the valence band, may be the cause of the somewhat smaller band gap in $NdNiO_3$. When compared to $CoNiO_2$, $NdNiO_3$ exhibits better electrochemical activity, which might be attributed to these flaws that increase charge carrier mobility.

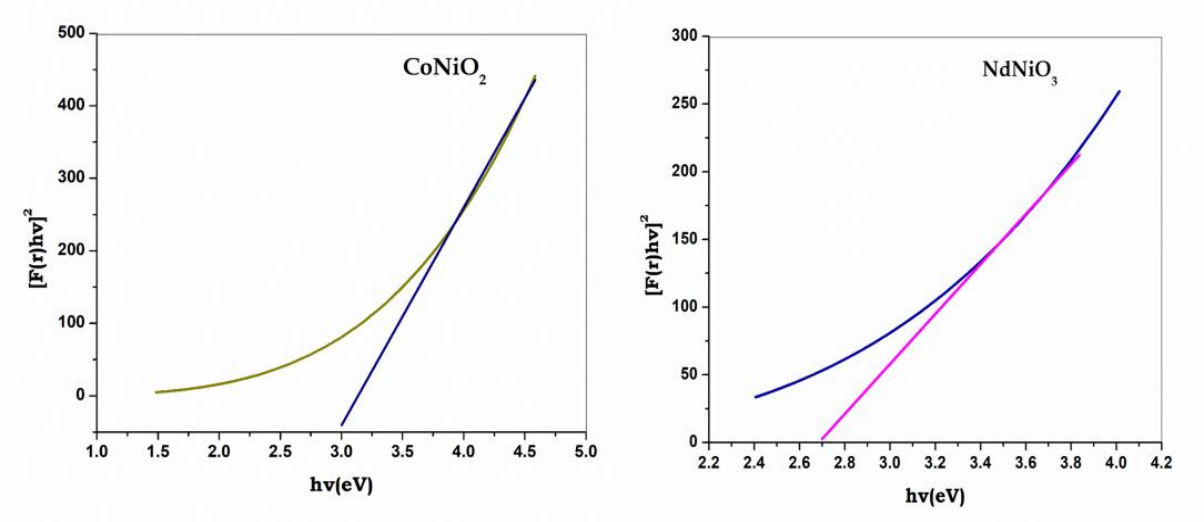

Fig.5 Tauc Plot of (a) $CoNiO_2$ and (b) $NdNiO_3$

XPS Analysis of $CoNiO_2$

The elements cobalt (Co), nickel (Ni), carbon (C), and oxygen (O) are present in the $CoNiO_2$ nanocomposite, according to the X-ray photoelectron spectroscopy (XPS) survey spectrum displayed in Fig. 6a. The exceptional purity of the synthesised substance is confirmed by the lack of signals from other elements. High-resolution scans produced additional information on the chemical

Journal of Chemical Health Risks
www.jchr.org
JCHR (2026) 16(2), 2917 - 2930

states of the constituent elements, as shown in Fig. 6b–6e.

The Ni $2p_{3/2}$ and Ni $2p_{1/2}$ spin-orbit components are represented by two conspicuous peaks in the deconvoluted Ni 2p spectra in Figure 6b, which are situated at binding energies of 855.3 eV and 873.6 eV, respectively. The Co 2p spectra is shown in Fig. 6c, with peaks at 781.0 eV and 796.2 eV corresponding to Co $2p_{3/2}$ and Co $2p_{1/2}$, respectively, signifying the cobalt oxidation states in the composite. A peak at 285.2 eV in the C 1s core-level spectrum (Fig. 6d) is commonly linked to carbon species and is most likely the result of the decreased graphene oxide concentration. Furthermore, a peak located at 531.4 eV in the O 1s spectra seen in Fig. 6e is often attributed to oxygen-containing functional groups and surface-adsorbed water (H–O–H). These spectrum characteristics attest to the $CoNiO_2$ nanocomposite's successful synthesis and surface composition.

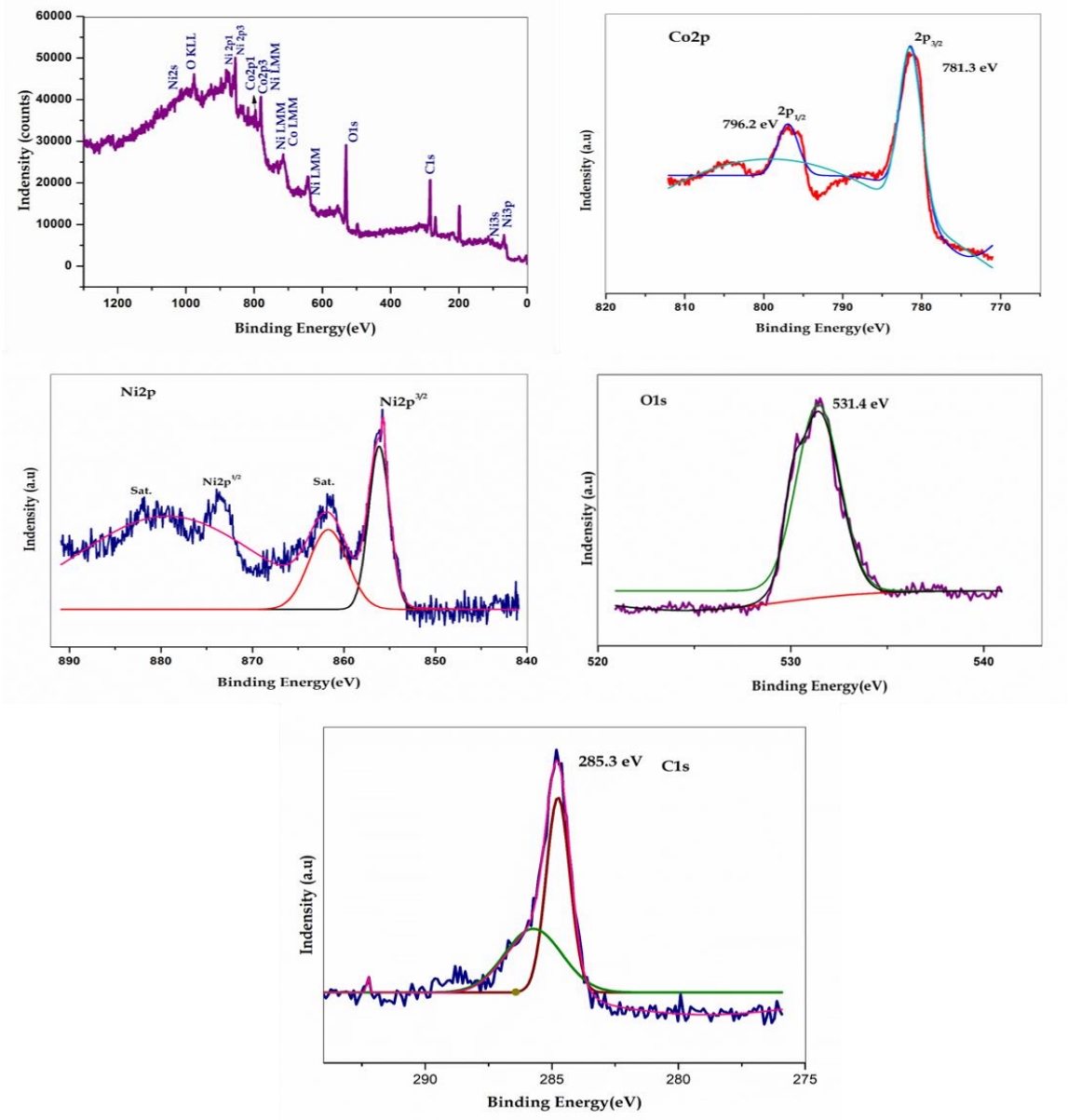

Fig.6 XPS spectra of $CoNiO_2$ nanocomposite (a) Survey spectrum, (b) Ni2p core spectrum, (c)Co2p core spectrum, (d) O1s core spectrum and (e) C1s core spectrum

Journal of Chemical Health Risks

www.jchr.org

JCHR (2026) 16(2), 2917 - 2930

XPS Analysis of $NdNiO_3$

X-ray photoelectron spectroscopy (XPS) was used to examine the $NdNiO_3$ nanocomposite's oxidation states and surface chemical composition. With no indication of additional elements, the whole survey spectrum, shown in Fig. 7a, verifies the existence of neodymium (Nd 3d), nickel (Ni 2p), oxygen (O 1s), and carbon (C 1s) signals, demonstrating the material's purity. As seen in Fig. 7b–7e, the core level spectra were deconvoluted using Gaussian fitting in order to further analyze the various elemental states.

The Nd 3d spectrum in Figure 7b shows two distinct peaks at binding energies of 1003.0 eV and 981.6 eV, respectively. These peaks represent the Nd $3d_{3/2}$ and Nd $3d_{3/2}$ components. The oxidation status of neodymium in the composite is confirmed by these measurements. The presence of nickel in the +2-oxidation state is suggested by the major peak at 872.2 eV in the Ni 2p core level spectra (Fig. 7c), which is attributed to Ni $2p_{3/2}$. A peak at 530.7 eV in the O 1s spectrum (Fig. 7d) is commonly linked to lattice oxygen in the $NdNiO_3$ structure [18]. The C–C and C–O bonds are indicated by the major peak at 284.3 eV in the C 1s spectra, which is shown in Fig. 7e. Since most oxygen functionalities are removed during synthesis, the comparatively low intensity of oxygen-containing functional groups in the C 1s area points to an efficient reduction mechanism.

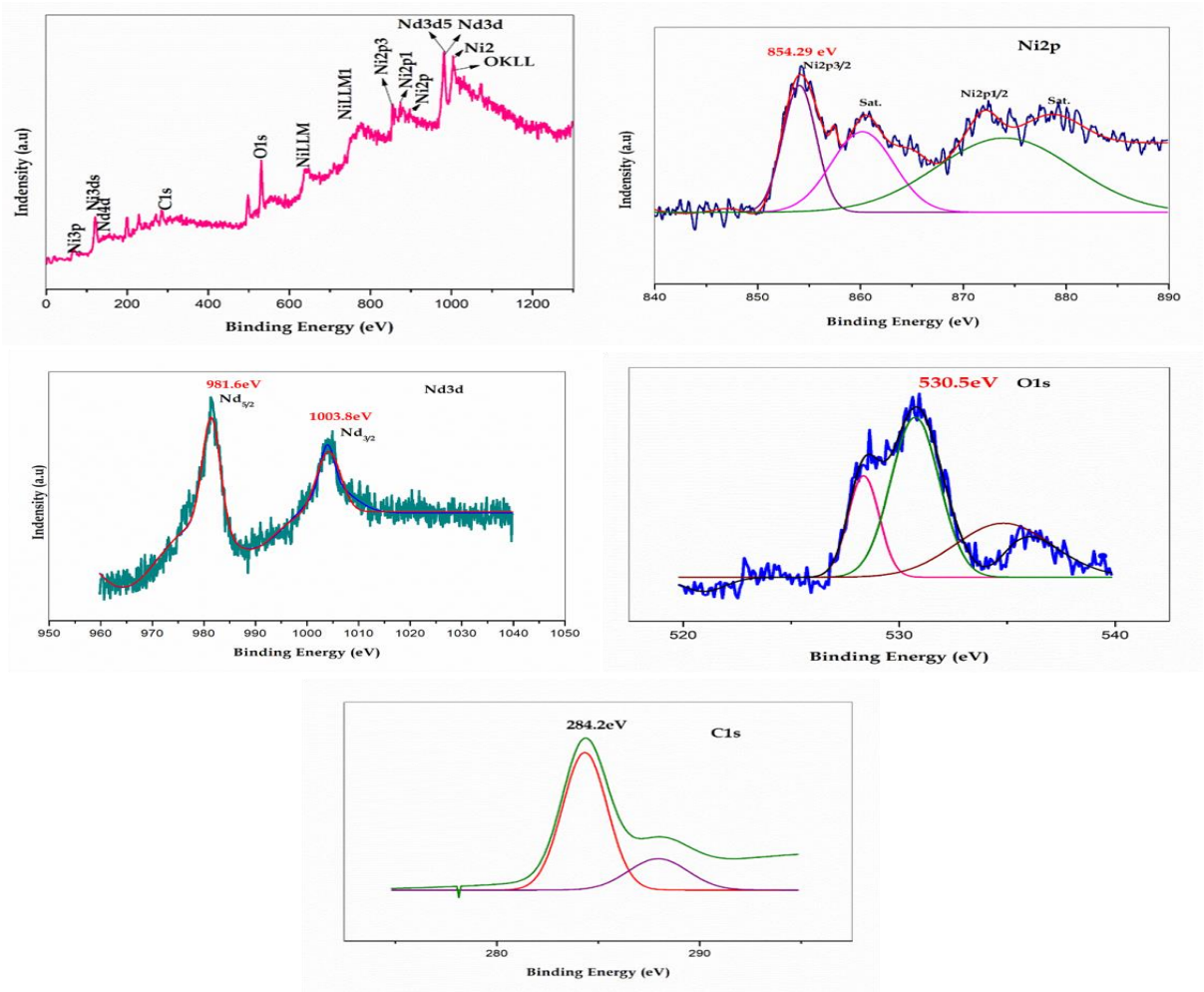

Fig.7 XPS spectra of $NdNiO_3$ nanocomposite (a) Survey spectrum, (b) Nd3d core spectrum, (c)Ni2p core spectrum, (d) O1s core spectrum and (e) C1s core spectrum

Journal of Chemical Health Risks
www.jchr.org
JCHR (2026) 16(2), 2917 - 2930

Electro chemical analysis

CV, GCD, and EIS are used to assess the $CoNiO_2$ and $NdNiO_3$ electrodes' electrochemical performance. A 1M KOH electrolyte solution was used to carry out the electrochemical performance between -0.13 and 0.5 V. The CV curves for the $CoNiO_2$ and $NdNiO_3$ electrodes with varying scan rates—10, 20, 50, 75, and 100 mV/s—are displayed in Figures 20a and 20b. The characteristic oxidation and reduction peaks seen in the $CoNiO_2$ and $NdNiO_3$ electrodes on the CV curve demonstrated the electrodes' pseudo capacitance. According to Fig. 20a, the voltammogram's shape remained constant even at a higher scan rate, demonstrating the electrode's exceptional reversibility and the quick transport of electrons towards the scan rate.

Fig.8. CV mechanism of $CoNiO_2$ and $NdNiO_3$ electrodes

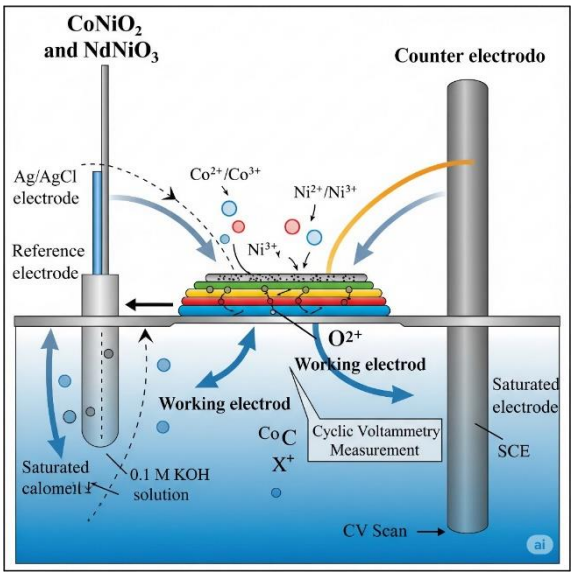

Furthermore, in relation to scan rate, the oxidation and reduction peaks are moved towards a greater current response. Composite electrodes such as $NdNiO_3$ have a significantly greater current responsiveness in relation to scan rates as compared to pure $CoNiO_2$ electrodes. The rapid insertion and exertion of electrolyte ions through the diffusion channels created by the graphene nanosheet and $CoNiO_2$ electrode combination resulted in an increase in specific capacitance. This might be the $NdNiO_3$ electrode's synergistic impact.

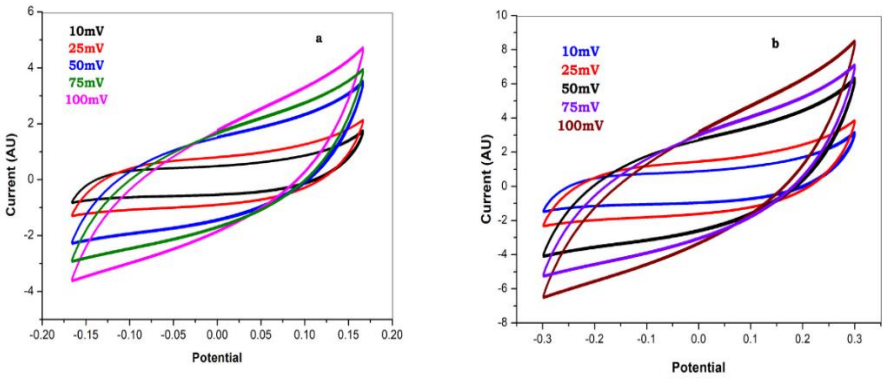

Fig.9. CV curves a) $CoNiO_2$ and b) $NdNiO_3$ electrodes

Journal of Chemical Health Risks

www.jchr.org

JCHR (2026) 16(2), 2917 - 2930

Equation 6 and the values in Table 4 were used to determine the specific capacitance values of the prepared $CoNiO_2$ & $NdNiO_3$ electrodes. Because there is less time for interaction between the electrode and the electrolyte solution at higher scan rates, the specific capacitance values of the produced electrodes gradually drop as the scan rate increases (Fig. 9a, Fig. 9b). It is evident that the $NdNiO_3$ electrode's specific capacitance values (499.7 F/g at 10 mV/s) are significantly greater than those of the $CoNiO_2$ electrode (158.8 F/g at 10 mV/s).

$$C_s = \frac{s}{mk\Delta V} \qquad \text{------- 6}$$

Table.4 Specific capacitance for $CoSnO_3$ & $NdNiO_3$ electrodes

Scan rate (mVs^{-1})	**Specific capacitance (Fg^{-1})**	
	$CoNiO_2$	$NdNiO_3$
10	158.8485	499.725
25	128.0758	342.737
50	83.61212	223.75
75	63.53535	170.033
100	51.40303	137.581

Galvanostatic charge/discharge analyses were also conducted to evaluate the super capacitive performance of the electrode. Fig.9a and Fig.b illustrates the charge/discharge curves for the $CoNiO_2$ and $NdNiO_3$ electrodes in the potential window of -0.13 to 0.5 V at various current rates from 1, 3, 5 and 7 A/g. The results reveal that the curves for the $CoNiO_2$ and $NdNiO_3$ electrodes are triangular, linear, symmetric and very sharp. Moreover, the discharge time responses of the $NdNiO_3$ electrodes were much higher than the pure electrode, which is mainly due to the synergistic effect of $NdNiO_3$ for its high surface area and high conductivity. The specific capacitance values of the prepared electrodes were estimated and reproduced in Table 5.

The specific capacitance values of the prepared $CoNiO_2$ and $NdNiO_3$ electrodes for varying current densities are displayed in Table 5. The $CoNiO_2$ and $NdNiO_3$ electrodes show high specific capacitance values at a reduced current density of 1A/g, according to Table 5. Additionally, when the current density increases, the prepared electrodes' specific capacitance values drop [108]. Furthermore, the presence of rGO in the produced electrodes is the primary reason why the specific capacitance values of the $NdNiO_3$ (603 F/g at 1 A/g) electrode are significantly greater than those of the $CoNiO_2$ (285 F/g at 1 A/g) electrode.

Table.1 Specific capacitance for $CoNiO_2$ and $NdNiO_3$ electrode using GCD curve

Current density A/g	**Specific capacitance (Fg^{-1})**	
	$CoNiO_2$	$NdNiO_3$
1	285.345	603.125
3	143.134	546.231

Journal of Chemical Health Risks
www.jchr.org
JCHR (2026) 16(2), 2917 - 2930

5	98.521	324.345
7	86.428	183.264

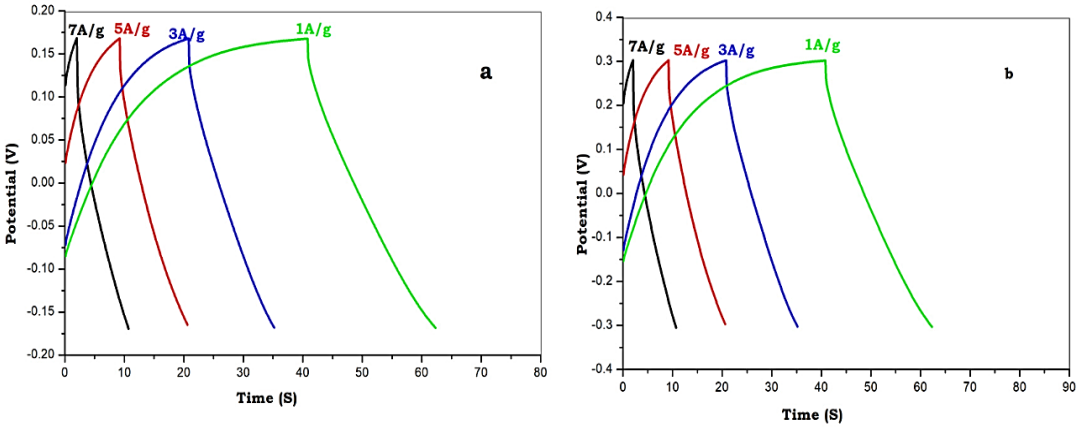

Fig.10. GCD curve of a) $CoNiO_2$ and b) $NdNiO_3$ electrodes

EIS spectra were used to characterize the electrodes' internal and exterior resistance as well as the interaction between the electrode and electrolytes. The frequency range for the EIS analysis recording was 0.1 Hz to 100 kHz. The EIS curves for the $CoNiO_2$ and $NdNiO_3$ electrodes are displayed in Figures 22a and b. Two frequency areas may be identified from the EIS curves: a low frequency region (straight line) and a high frequency region (semicircle). The low resistivity of the $NdNiO_3$ electrodes is indicated by the fact that their semicircle is significantly smaller than that of $CoNiO_2$. A Nyquist plot usually shows one straight line and one semicircle. The bulk electrolyte resistance is indicated by the semicircle at a higher frequency, and the electrode resistance is indicated by the straight line at a lower frequency.

Additionally, the Z-fit analysis was fitted to the Nyquist plot, revealing that the $CoNiO_2$ and $NdNiO_3$ electrodes had charge transfer resistance values of 3.6 and 2.4 ohm, respectively. This suggests that the $CoNiO_2$ can offer excellent conductivity and lower the resistivity of the manufactured $CoSnO_3$ electrode since the charge transfer resistance values of the $NdNiO_3$ electrode are lower than those of the pure $CoNiO_2$ electrode.

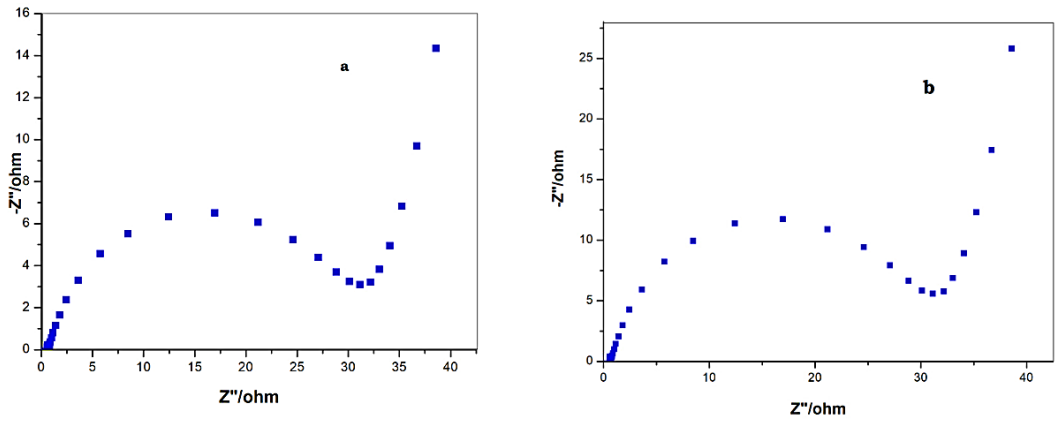

Fig.9 EIS spectra of $CoNiO_2$ and $NdNiO_3$

Journal of Chemical Health Risks

www.jchr.org

JCHR (2026) 16(2), 2917 - 2930

Conclusion:

The nanomaterials NiO, $CoNiO_2$, and $NdNiO_3$ were synthesized using the hydrothermal method. After six hours of calcination at 450°C, the produced materials yielded nanomaterials of NiO, $CoNiO_2$, $NdNiO_3$, and $CoNiO_2$ with crystalline sizes of 19.8, 43.5, 46.3, 56.2, 50.4, and 64.5 nm. SEM analysis of the surface morphology showed that the surface of rGO with a 2D sheet structure is covered with agglomerated $CoNiO_2$ and flower-shaped $NdNiO_3$ nanoparticles. The band gaps of $CoNiO_2$ and $NdNiO_3$ were examined using a Kubelka-Munk function plot at 3.0 and 2.7 eV, respectively. In comparison to the $CoNiO_2$ (90%) nanocomposite, the $NdNiO_3$ nanocomposite exhibits a higher electrochemical property (95%) in terms of electrochemical performance.

Reference:

1. Haanappel, V. A. C., Lalanne, C., Mai, A., & Tietz, F. (2009). *Characterization* of anode-supported solid oxide fuel cells with Nd_2NiO_4 cathodes. *Journal of Fuel Cell Science and Technology*, *6*(4).
2. Rodríguez-González, V., Terashima, C., & Fujishima, A. (2019). Applications of photocatalytic titanium dioxide-based nanomaterials in sustainable agriculture. *Journal of Photochemistry and Photobiology C: Photochemistry Reviews*, *40*, 49-67.
3. Narayanan, D. P., Gopalakrishnan, A., Yaakob, Z., Sugunan, S., & Narayanan, B. N. (2020). A facile synthesis of clay–graphene oxide nanocomposite catalysts for solvent free multicomponent Biginelli reaction. *Arabian Journal of Chemistry*, *13*(1), 318-334.
4. Adetayo, A., & Runsewe, D. (2019). Synthesis and fabrication of graphene and graphene oxide: A review. *Open Journal of Composite Materials*, *9*(02), 207.
5. Shen, H., Wang, Y. Z., Liu, G., Li, L., Xia, R., Luo, B., ... & Yong, Y. C. (2020). A whole-cell inorganic-biohybrid system integrated by reduced graphene oxide for boosting solar hydrogen production. *Acs Catalysis*, *10*(22), 13290-13295.
6. Luo, L., Yang, M., & Chen, G. (2020). Continuous synthesis of reduced graphene oxide-supported bimetallic NPs in liquid–liquid segmented flow. *Industrial & Engineering Chemistry Research*, *59*(17), 8456-8468.
7. Jana, A., Scheer, E., & Polarz, S. (2017). Synthesis of graphene–transition metal oxide hybrid nanoparticles and their application in various fields. *Beilstein Journal of Nanotechnology*, *8*(1), 688-714.
8. Dideikin, A. T., & Vul, A. Y. (2019). Graphene oxide and derivatives: the place in graphene family. *Frontiers in Physics*, *6*, 149.
9. Zakaria, M. B., Zheng, D., Apfel, U. P., Nagata, T., Kenawy, E. R. S., & Lin, J. (2020). Dual-heteroatom-doped reduced graphene oxide sheets conjoined CoNi-based carbide and sulfide nanoparticles for efficient oxygen evolution reaction. *ACS Applied Materials & Interfaces*, *12*(36), 40186-40193.
10. Kawahara, A., & Ishihara, T. (2010). Oxygen permeation property in Nd Deficient Nd_2NiO_4 mixed oxide doped with Cu and Ga. *Electrochemical and Solid-State Letters*, *13*(7), B76.
11. Buttrey, D. J., & Honig, J. M. (1988). Influence of nonstoichiometry on the magnetic properties of Pr_2NiO_4 and Nd_2NiO_4. *Journal of Solid-State Chemistry*, *72*(1), 38-41.
12. Puche, R. S., Fernández, F., Carvajal, J. R., & Martinez, J. L. (1989). Magnetic and X-ray diffraction characterization of stoichiometric Pr_2NiO_4 and Nd_2NiO_4 oxides. *Solid State Communications*, *72*(3), 273-277.
13. Castro, M., & Burriel, R. (1995). Phase transitions and crystal-field levels in Nd_2NiO_4. *Thermochimica Acta*, *269*, 523-535.
14. Ai, Yuanfei, et al. "Rational synthesis of branched $CoMoO_4$@ $CoNiO_2$ core/shell nanowire arrays for all-solid-state supercapacitors with improved performance." *ACS applied materials & interfaces* 7.43 (2015): 24204-24211.
15. Du, Weimin, et al. "One-pot synthesis of $CoNiO_2$ single-crystalline nanoparticles as high-performance electrode materials of asymmetric supercapacitors." *Journal of Nanoparticle Research* 17.9 (2015): 368.
16. Yi, T-F., et al. "Toward high-performance Li storage anodes: design and construction of

spherical carbon-coated $CoNiO_2$ materials." *Materials Today Chemistry* 19 (2021): 100407.

17. Yao, Jianyu, et al. "CoNiO nanowire arrays as a high-performance anode material for lithium-ion batteries." *Journal of alloys and compounds* 583 (2014): 366-371.
18. Jiang, Yan, et al. "Synthesis of bimebtallic CoNi-CoNiO2 nanoparticles embedded into mesoporous carbon as high-performance catalysts for supercapacitor electrode." *Microporous and Mesoporous Materials* 272 (2018): 222-231.
19. Guan, Yayu, et al. "Facile synthesis of double-layered $CoNiO_2$/CoO nanowire arrays as multifunction electrodes for hydrogen electrocatalysis and supercapacitors." *Electrochimica Acta* 342 (2020): 136093.
20. Zhang, Jijun, et al. "Morphology-controllable synthesis of 3D CoNiO2 nano-networks as a high-performance positive electrode material for supercapacitors." *Energy* 113 (2016): 943-948.
21. Firdous, Zarghuna, et al. "Enhancement of electrochemical performance of hydrothermally synthesized CoNiO2/PANI for OER efficiency." *Chemical Physics* 595 (2025): 112728.
22. Ali Sheikh, Zulfqar, et al. "Formulation of hierarchical nanowire-structured $CoNiO_2$ and MoS_2/$CoNiO_2$ hybrid composite electrodes for supercapacitor applications." *ACS Applied Materials & Interfaces* 16.8 (2024): 10104-10115.